Correlations and incipient antiferromagnetic order within the linear Mn chains of metallic Ti_4MnBi_2

Abhishek Pandey,[1,2,*] Ping Miao,[2] M. Klemm,[2] H. He,[2] H. Wang,[3] X. Qian,[3] J. W. Lynn,[4] and M. C. Aronson[2,3,5,6,†]

[1]*School of Physics, University of the Witwatersrand, Johannesburg, Gauteng 2050, South Africa*
[2]*Department of Physics and Astronomy, Texas A&M University, College Station, Texas 77843, USA*
[3]*Department of Materials Science and Engineering, Texas A&M University, College Station, Texas 77843, USA*
[4]*NIST Center for Neutron Research, National Institute of Standards and Technology, Gaithersburg, Maryland 20899, USA*
[5]*Department of Physics and Astronomy, University of British Columbia, Vancouver, British Columbia, Canada V6T 1Z4*
[6]*Stewart Blusson Quantum Matter Institute, University of British Columbia, Vancouver, British Columbia, Canada V6T 1Z4*

(Received 7 January 2020; revised 18 May 2020; accepted 15 June 2020; published 6 July 2020)

We report measurements on Ti_4MnBi_2, where a crystal structure involving linear chains of Mn ions suggests one-dimensional magnetic character. The electrical resistivity is metallic, consistent with the results of electronic-structure calculations that find a robust Fermi surface albeit with moderate electronic correlations. A Curie-Weiss fit to the magnetic susceptibility suggests that the Mn moments are in the low-spin $S = 1/2$ configuration. Neutron diffraction measurements detect weak antiferromagnetic order within the Mn chains, with further evidence for the small staggered moment coming from the entropy associated with the ordering peak in the specific heat as well as from the results of spin-polarized electronic-structure calculations. The antiferromagnetic moments are apparently associated with the $d_{x^2-y^2}$ and d_{xy} orbitals of Mn while the remaining Mn orbitals are delocalized and nonmagnetic. Strong quantum fluctuations, possibly related to an electronic instability that forms the Mn moment or to the one-dimensional character of Ti_4MnBi_2, nearly overcome magnetic order.

DOI: 10.1103/PhysRevB.102.014406

I. INTRODUCTION

Low-dimensional magnetic systems continue to excite since strong quantum fluctuations suppress magnetic order, showcasing quantum effects at the lowest temperatures [1]. Of particular importance is the extensive body of theoretical results on one-dimensional (1D) systems that can be directly tested by experiments like inelastic neutron scattering [2,3] and resonant inelastic x-ray scattering [4]. To date, most experiments have been carried out on spin $S = 1/2$ systems like $KCuF_3$ [5–8], $SrCuO_2$ [9], Sr_2CuO_3 [10], and $CuSO_4.5D_2O$ [3], which are strongly correlated insulators. Inelastic neutron scattering experiments demonstrate that the fundamental excitations are not the spin waves expected in three-dimensional (3D) systems, but rather spinons, demonstrating that the electron spin and charge have become separated [6,11,12].

It is less clear what happens to this scenario when electronic correlations are not strong enough to sustain an insulating gap. The first examples of metallic spin chains were the organic conductors [13–15], where the ratio of the Coulomb interaction U and the electron bandwidth $4t$ are approximately equal, i.e., $U/4t \simeq 1$. Angle-resolved photoemission spectroscopic (ARPES) measurements found that the fundamental excitations are gapless spinons and holons in the organic conductor tetrathiafulvalene tetracyanoquinodimethan (TTF-TCNQ) [16], confirming theoretical expectations that 1D metals are Tomonaga-Luttinger liquids [1]. Although electronic interactions and interchain coupling can be sufficiently strong in organic conductors [13–15] to drive many-body ground states like superconductivity, magnetic order, or even metal-insulator transitions, these materials are mechanically fragile and are only available in small quantities. As a result, it is problematic to utilize the most powerful spectroscopic tools, in particular, inelastic neutron scattering measurements, on these materials. There remains a pressing need to identify new families of compounds with metallic spin chains where the impact of intermediate electronic interactions may be assessed. In particular, the near absence of suitable 1D materials has meant that the interplay of magnetic correlations and Kondo compensation of the underlying moments, central to the rich physics of the 3D heavy fermions, remains virtually unexplored by experiments in their 1D counterparts [17–21]. We report here measurements on an unexplored metallic system Ti_4MnBi_2 that suggest the 1D character implied by its unique crystal structure may control its fundamental properties.

Ti_4MnBi_2 has a remarkable crystal structure [22,23] with well-separated linear chains of Mn ions. Electrical resistivity measurements demonstrate that Ti_4MnBi_2 is a metal and electronic-structure calculations (ESC) confirm that there is a robust Fermi surface with moderate mass enhancement. The magnetic susceptibility measurements lead to a Curie-Weiss (CW) magnetic moment with a magnitude of 1.79 μ_B/Mn and also suggest antiferromagnetic (AFM) order near 2 K. However, the ordered moment is much smaller than the CW moment, indicating that quantum fluctuations are likely quite strong in Ti_4MnBi_2, possibly due to its 1D character or, alternatively, to proximity to an electronic instability that produces the magnetic moment itself. Our measurements suggest that d-electron-based intermetallic compounds like

*abhishek.pandey@wits.ac.za
†meigan.aronson@ubc.ca

Ti_4MnBi_2 are likely a productive direction to explore, in which robust magnetic chains are embedded in metallic hosts.

II. EXPERIMENTAL AND COMPUTATIONAL DETAILS

Single crystals of Ti_4MnBi_2 were grown using the solution growth technique. High purity Ti (99.99%), Mn (99.98%), and Bi (99.999%) in the molar ratio of 4:2:10 were placed in an alumina crucible and sealed inside an evacuated quartz tube. The assembly was heated to 1150 °C in 10 h, kept there for 30 h, and then cooled down to 800 °C in 100 h. At this temperature, the excess Bi-flux was decanted and needle like crystals of typical size $0.5 \times 0.5 \times 3$ mm^3 were obtained.

Structural characterization of the compound was performed using single crystal and powder x-ray diffraction (XRD). The single-crystal diffraction intensity data were collected at room temperature using a Bruker D8 Quest diffractometer with Mo-K_α radiation ($\lambda = 0.71073$ Å). Data integration/reduction and an absorption correction using a multiscan method were performed with the BRUKER APEX2 software suite. The structure was solved by the direct method and refined by a full matrix least-squares method against F2 using the SHELX package. Room-temperature powder XRD data were obtained on a few crushed crystals using a Bruker D8 Advance Powder Diffractometer employing Cu-K_α radiation. Rietveld refinement was carried out using the FULLPROF [24] package, keeping the occupancies at each lattice site fixed at 100%. A satisfactory refinement of the room-temperature powder XRD data, as shown in Fig. S1 of the Supplemental Material [25], confirms the single phase nature of the material, the integral site occupancies, and the absence of any measurable site disorder. A similar conclusion was reached by refinement of the single-crystal XRD data.

Magnetic measurements at different temperatures $0.45\ \text{K} \leqslant T \leqslant 300\ \text{K}$ and magnetic fields $H \leqslant 70$ kOe ($1\ \text{Oe} = 1000/4\pi$ A/m) were carried out using a Quantum Design Inc. Magnetic Properties Measurement System fitted with a ^{3}He option as well as a vibrating sample magnetometer installed in a Physical Properties Measurement System (PPMS) of the same manufacture. Measurements of heat capacity $C_p(T)$ and c-axis electrical resistivity $\rho_c(T)$ were performed using the ^{3}He option of PPMS. In the latter experiment, contacts were made using silver-filled epoxy and the measuring current was 500 μA.

Neutron powder-diffraction data were collected on a 4 g powder sample prepared by crushing single crystals of Ti_4MnBi_2. The data were obtained with a neutron wavelength of 2.359 Å using the double focusing triple-axis spectrometer BT-7 at the NIST Center for Neutron Research [26], which is equipped with position-sensitive detectors and a dilution refrigerator with a base temperature of 0.05 K. Rietveld refinement of these data was performed using the software Z-RIETVELD [27,28]. The residual value of R_{wp} was below 10%. In addition, single-crystal neutron diffraction measurements were performed on BT-7 using 2 g aligned single crystals of Ti_4MnBi_2 mounted in a closed-cycle refrigeration unit that obtains temperatures below 2.5 K. Uncertainties, where indicated, represent one standard deviation.

The electronic structure of Ti_4MnBi_2 was calculated using first-principles density-functional theory [29,30] as implemented in the VIENNA AB INITIO SIMULATION PACKAGE [31] with the projector-augmented wave method [32]. We employed the Perdew-Burke-Ernzerhof exchange-correlation functional [33], a plane-wave basis with an energy cutoff of 200 eV, and a Monkhorst-Pack k-point sampling of $4 \times 4 \times 4$ for Brillouin zone integration [34] as well as spin-orbit coupling. A Hubbard U correction [35] of $U_{\text{eff}} = 3.9$ eV was applied to treat the strong Coulomb interactions of localized d-electrons on the Mn atoms.

TABLE I. Room-temperature crystallographic parameters estimated from x-ray powder diffraction data of tetragonal Ti_4MnBi_2, which crystallizes in a V_4SiSb_2-type structure with $I4/mcm$ (No. 140) space-group symmetry and $Z = 4$ formula units/cell.

Atom	Wyckoff Position	x	y	z
Ti	16k	0.0804(3)	0.1977(4)	0
Mn	4a	0	0	$\frac{1}{4}$
Bi	8h	0.1390(1)	0.6390(1)	0
Lattice parameters				
a (Å)	10.4946(4)			
c (Å)	4.9860(2)			
c/a	0.47510(4)			
V_{cell} (Å^3)	549.14(4)			
$d_{\text{Mn-Mn}}$ (Å)	2.4930(1)			
d_{chain} (Å)	7.4208(3)			

III. RESULTS

A. Structural properties

Ti_4MnBi_2 has been previously reported to form in the V_4SiSb_2-type tetragonal structure (space group $I4/mcm$, No. 140) [22,23], and the structural parameters obtained from our XRD refinements (Table I) are in good agreement with the published results. The crystal structure of Ti_4MnBi_2 depicted in Fig. 1 emphasizes its 1D character. Linear chains of Mn atoms with a Mn-Mn spacing of $d_{\text{Mn-Mn}} = 2.4930(1)$ Å extend along the tetragonal c-axis. The Mn chains are encased along the c direction in concentric tubes with an inner tube of Ti atoms and a larger diameter tube of Bi atoms [Fig. 1(a)]. The distance between Mn chains $d_{\text{chain}} = 7.4208(3)$ Å is substantially larger than $d_{\text{Mn-Mn}}$ [Fig. 1(b)], suggesting a possible one-dimensionality of the Mn subsystem. The Mn ions are centered in square-antiprism coordination polyhedra of Ti-ions [Fig. 1(c)].

B. Electrical resistivity

We begin by establishing that Ti_4MnBi_2 is intrinsically metallic. The temperature dependence of the c-axis electrical resistivity $\rho_c(T)$ measured for temperatures between 0.5−300 K is presented in Fig. 2. Similar results were obtained on multiple crystals, with little variation in the residual resistivity ρ_0, which was found to vary between 100−120 $\mu\Omega$ cm. The overall good quality of our single crystals and the lack of significant sample dependence suggest that disorder is unlikely to be solely responsible for the large value of ρ_0, implying that other sorts of scattering processes

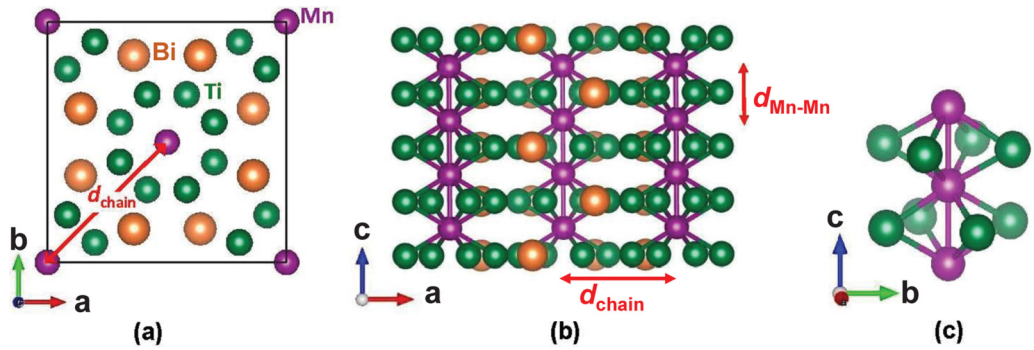

FIG. 1. Crystal structure of tetragonal Ti_4MnBi_2. (a) A view of the crystal structure in the basal plane, depicting the central Mn ion surrounded by an inner ring of eight Ti ions and an outer ring of eight Bi ions. The respective rings of Ti and Bi ions are formed by two sets of four coplanar ions occupying the corners of square-planer lattices that are separated by $d = c/2$ along the c-axis and are at an angle of 45° with respect to each other. Extending along the c-axis, these rings constitute tubelike structures of Ti and Bi that surround the linear chains of Mn ions. (b) A view of the two unit cells of Ti_4MnBi_2 stacked on the top of each other along the c-axis. It is evident from (a) and (b) that the Mn ions form linear chains running along the c-axis of the tetragonal unit cell. The interchain distance between the two nearest Mn ions within the ab-plane is $d_{chain} = a/\sqrt{2} = 7.4208(3)$ Å and the intrachain distance between the two neighboring Mn ions is $d_{Mn\text{-}Mn} = c/2 = 2.4930(1)$ Å. (c) The Mn ions centered in a square-antiprism coordination polyhedra of Ti ions. Two nearest-neighbor Mn ions capping the respective square faces are also shown.

including quantum fluctuations may be present at $T = 0$. A metallic temperature dependence was found at all temperatures $0.5\ K \leqslant T \leqslant 300\ K$, with $\rho_c(T)$ increasing monotonically with increasing temperature. Fermi liquid behavior was found for $T \lesssim 75\ K$ [inset, Fig. 2], where the resistivity data were fitted by $\rho_c = \rho_0 + AT^2$, with $A = 1.103(3) \times 10^{-3}\ \mu\Omega$ cm/K^2 (Table II). This value of A is enhanced relative to values found in simple metals and is similar to those found in correlated d-electron compounds like $La_{1.7}Sr_{0.3}CuO_4$ and Sr_2RuO_4 [36]. This is our first indication that the conduction electrons in Ti_4MnBi_2 are significantly correlated.

At higher temperatures, $\rho_c(T)$ does not approach the linear temperature dependence that is expected in the Bloch-Grüneisen model of conduction carrier scattering from acoustic lattice vibrations. A pronounced downward curvature is observed and a satisfactory fitting of the data is obtained by

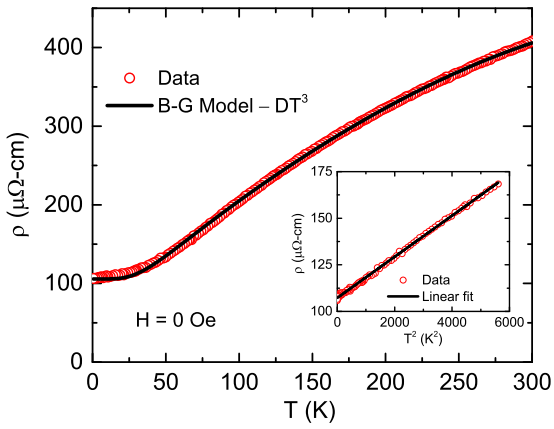

FIG. 2. Temperature dependence of the electrical resistivity $\rho_c(T)$ of Ti_4MnBi_2 measured along the crystallographic c-axis. The solid black curve is a fit by the Bloch-Grüneisen model with an additional term $-DT^3$ ascribed to Mott sd-scattering (see text). Inset: ρ_c plotted as a function of temperature squared T^2 for $T \lesssim 75$ K. Solid black line is a linear fit to the data.

TABLE II. Parameters deduced from electronic structure calculations as well as magnetic, thermal, and electrical transport measurements performed on Ti_4MnBi_2 single crystals, where C is the Curie constant, μ_{eff} is the effective paramagnetic moment, θ_p is the paramagnetic wise temperature, J_c is the nearest-neighbor exchange constant along the c-axis, χ_0 is the temperature independent susceptibility estimated from the CW fit, χ_{Pauli} is the Pauli susceptibility estimated from the experimental value of the Sommerfeld coefficient γ, β is the coefficient of lattice heat capacity at low temperatures, $\mathcal{D}_\gamma$ (states/eV f.u.) for both spin directions is the density of states (DOS) at the Fermi level E_F deduced from the γ value, $\mathcal{D}_{band}$ (states/eV f.u.) for both spin directions is the DOS at E_F calculated by electronic-structure calculations, Θ_D and Θ_E are Debye and Einstein temperatures estimated from heat capacity data, respectively, u is the fraction of Debye contribution to the heat capacity, A is the coefficient of T^2 term in of the resistivity data at low temperatures, D is the coefficient of Mott sd-scattering term in the resistivity data, R_{KW} (mΩ cm mol^2 J^{-2}K^2) is the Kadowaki-Woods ratio, and R_W is the Wilson ratio.

Parameter	Estimated value
C (cm^3 K/mol)	0.41(2)
μ_{eff} (μ_B)	1.79(4)
θ_p (K)	−9(3)
J_c(K)	18(6)
χ_0 (10^{-4} cm^3/mol)	4.8(5)
χ_{Pauli} (10^{-4} cm^3/mol)	7.8(9)
γ (mJ/mol K^2)	57(5)
β (mJ/mol K^4)	0.94(6)
$\mathcal{D}_\gamma(E_F)$ (unit in the caption)	24(3)
$\mathcal{D}_{band}(E_F)$ (unit in the caption)	7.4(1)
$\Theta_{D,\ HT}$ (K)	381(15)
$\Theta_{D,\ LT}$ (K)	355(2)
Θ_E (K)	110(22)
u (unitless)	0.73(7)
A (10^{-3} $\mu\Omega$ cm/K^2)	1.103(3)
D (10^{-8} $\mu\Omega$ cm/K^3)	2.43(3)
R_{KW} (unit in the caption)	3.4×10^{-4}
R_W (unitless)	0.6(2)

adding a Mott-*sd* scattering term $-DT^3$ with $D = 2.43(3) \times 10^{-8}$ $\mu\Omega\,\mathrm{cm/K^3}$ (Fig. 2). This is another piece of evidence for the presence of electronic correlations that originate with *d*-electrons.

C. Heat capacity and magnetic entropy

The temperature dependence of the specific heat $C_\mathrm{p}(T)$ for $0.45\ K \leqslant T \leqslant 266\ K$ is presented in Fig. 3(a). The value of C_p at 266 K is 161(1) J/mol K, which is ∼8% smaller than the Dulong-Petit limit of heat capacity at constant volume $C_\mathrm{V} = 3nR = 174.6$ J/mol K, where R is the gas constant and $n = 7$ is the number of atoms per formula unit. The most likely explanation for this shortfall is that the Debye temperature Θ_D of Ti_4MnBi_2 is significantly larger than 266 K. Using the Debye model to fit C_p(T) data was only partially successful, and it was necessary to add an Einstein term with a fraction $(1-u) = 0.27(7)$ of the total $C_\mathrm{p}(T)$ to fit the data (Table II), where u is the fractional contribution of the Debye term. With the above addition, we were able to satisfactorily fit the $C_\mathrm{p}(T)$ data [Fig. 3(a)] with the fitting parameters $\Theta_{\mathrm{D,\ HT}} = 381(15)$ K, the Debye temperature equivalent of the Einstein mode $\Theta_\mathrm{E} = 110(22)$ K, $u = 0.73(7)$, and $\gamma_\mathrm{HT} = 7(2)$ mJ/mol $\mathrm{K^2}$. As expected, the estimated value of $\Theta_{\mathrm{D,\ HT}}$ is significantly higher than room temperature.

The magnetic contributions to $C_\mathrm{p}(T)$ are most evident below ≃ 15 K, where the high-temperature fit discussed above shows a deviation from the measured data [Fig. 3(b)]. It is best isolated by comparing C_p/T to the low-temperature phonon contribution that is estimated by fitting $C_\mathrm{p}/T = \gamma + \beta T^2$ over the temperature range $10\ K \lesssim T \lesssim 18\ K$. This yields the Sommerfeld constant $\gamma = 57(5)$ mJ/mol $\mathrm{K^2}$ and $\beta = 0.94(6)$ mJ/mol $\mathrm{K^4}$ (Table II). The value of the low temperature γ is nearly an order of magnitude larger than the value γ_{HT} that is inferred at high temperature, suggesting the gradual onset of a correlated electron state with decreasing temperature in Ti_4MnBi_2. The value of $\Theta_{\mathrm{D,\ LT}}$ deduced from the fitted value of β is 355(2) K, in reasonable agreement with the value $\Theta_{\mathrm{D,\ HT}}$.

At the lowest temperatures, a broad peak centered at ≃1.9 K emerges in C_p/T [Fig. 3(b)]. It is possible that the peak corresponds to the onset of magnetic order, although the breadth of the peak suggests that the correlations associated with this putative order would be weak and short ranged. We have plotted in Fig. 3(c) the entropy S_mag associated with the magnetic part of the specific heat C_mag, which is obtained by subtracting the low-temperature phonon contribution βT^3 and electronic contribution γT from the measured specific heat, i.e., $C_\mathrm{mag} = C_\mathrm{p} - \beta T^3 - \gamma T$. The S_mag saturates to $0.09R\ln 2$ around 10 K. If the peak in the specific heat $C_\mathrm{p}(T)$ at 1.9 K is associated with magnetic ordering, then it is clear that the ordered moment is significantly smaller than the spin 1/2 moment whose entropy would be $R\ln 2$.

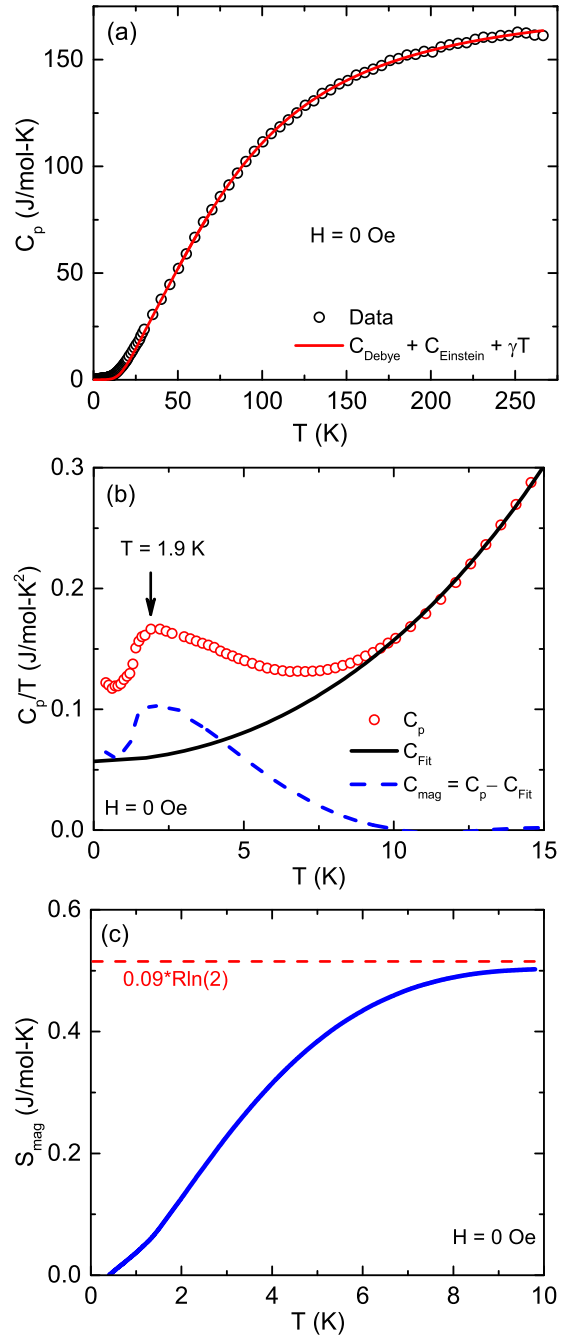

FIG. 3. (a) Temperature dependence of the molar heat capacity C_p. The solid curve is the fit including both the Debye model as well as a single-frequency Einstein oscillator, as described in the text. (b) Temperature dependence of $C_\mathrm{p}(T)/T$ for temperatures $0.45\ K \leqslant T \leqslant 15\ K$. Solid line is the fit $C_\mathrm{p}/T = \gamma + \beta T^2$, while the dashed curve is the difference of the experimental C_p/T and the fitted values. (c) Temperature dependence of the entropy $S_\mathrm{mag}(T) = \int_0^T \frac{\Delta C}{T} dT$ extracted from the $C_\mathrm{p}(T)$ data for $T \leqslant 10$ K. Horizontal dashed line represents 9% of the magnetic entropy $R\ln 2$ contained in a spin $S = 1/2$ system.

D. Electronic-structure calculations

The total and atom-decomposed electronic density of states (DOS) of Ti_4MnBi_2 are shown in Fig. 4(a). The compound is definitively metallic, having a sizable DOS $\mathcal{D}_\mathrm{band}(E_\mathrm{F}) = 7.4(1)$ states/(eV f.u.) for both spin directions at the Fermi energy E_F. To understand the contribution of the specific atoms to the DOS, we transformed the Kohn-Sham eigenstates of ESC into a set of highly localized quasiatomic orbitals. The eigenvalues of the Kohn-Sham wave functions were

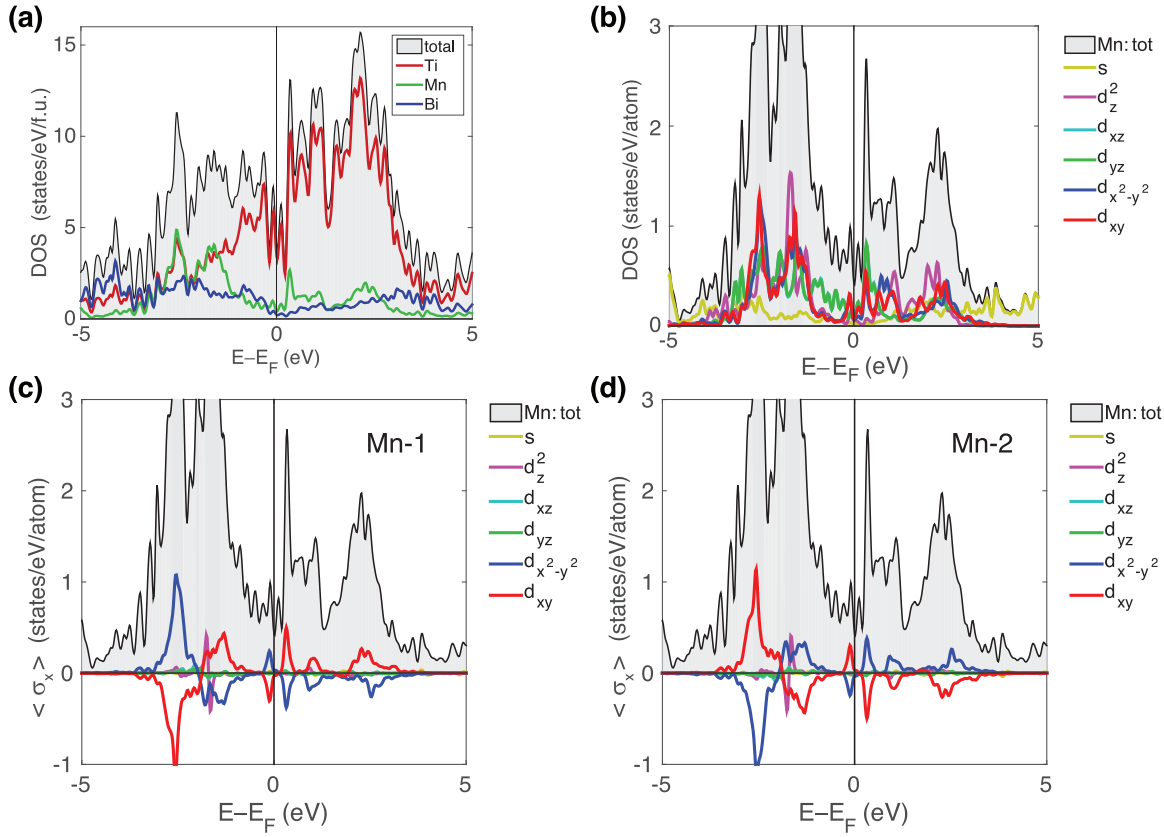

FIG. 4. (a) Atom-decomposed density of states (DOS) of Ti, Mn, and Bi as well as the total DOS, which clearly demonstrates that Ti contributes most of the DOS at the Fermi level. (b) Orbitally differentiated Mn states that are mostly centered around ±2.5 eV. The breadth of these states is comparable to their energies, indicating their pronounced itinerant character. To further understand the magnetic ordering, (c) and (d) show the the spin- and orbital-resolved DOS for two intrachain neighboring Mn atoms represented as Mn1 and Mn2, respectively, where σ_x indicates spin moment of the orbitals along the x direction. Only the d_{xy} and $d_{x^2-y^2}$ orbitals lying in the ab-plane have significant spin polarization. Antiferromagnetic order is predicted, since the spin polarization of these orbitals is opposite on neighboring Mn1 and Mn2 atoms.

transformed into a first-principles tight-binding Hamiltonian [37,38] which was subsequently used for computing the results. Figure 4(a) demonstrates that the Ti atoms contribute most of the DOS close to E_F, while the Mn and Bi atoms have much smaller shares. Within the accuracy of the ESC, none of the Mn d-orbitals makes a substantial contribution to the DOS at the E_F, which is instead dominated by the Ti states that appear to hybridize much more strongly with each other than with the Mn states.

Our measurements of the electrical resistivity and specific heat both suggest that the conduction electrons have significant electronic correlations at low temperatures. To further test this point, we estimated the DOS at E_F from the experimental value of γ,

$$\mathcal{D}_\gamma(E_F) = \frac{\pi^2 k_B^2}{3\gamma}, \tag{1}$$

that includes the many-body enhancement effects such as electron-electron and electron-phonon interactions. From the estimated γ of Ti_4MnBi_2 (Table II), we calculate $\mathcal{D}_\gamma(E_F) =$ 24(3) states/(eV f.u.) for both spin directions. The estimated $\mathcal{D}_\gamma(E_F)$ is significantly larger than the $\mathcal{D}_{band}(E_F) = 7.4(1)$ states/(eV f.u.) obtained from the ESC, confirming the presence of many-body enhancement effects in this material. We get $\mathcal{D}_\gamma(E_F)/\mathcal{D}_{band}(E_F) = \gamma/\gamma_{band} = (1 + \lambda_{el-ph})m^*/m_{band} =$ 3.2(5), where γ_{band} and m_{band} are band theory values of the Sommerfeld coefficient and conduction carrier effective mass and λ_{e-ph} is the electron phonon coupling constant. A factor of 3 enhancement in electron mass is in line with values computed and experimentally deduced for iron pnictides and chalcogenides [39] and also their Mn analogs [40–42].

The orbitally differentiated density of Mn states [Fig. 4(b)] is centered at $\simeq 2.5$ eV from E_F, reflecting the strength of the Coulomb and Hund's interactions that stabilize magnetic moments within the correlated Mn-based bands. Hybridization produces a substantial breadth to these states, extending from about -3 to $+3$ eV, indicating that charge and spin excitations are strong in Ti_4MnBi_2. Apparently, the Mn states are not fully localized and lack a stable valence, which is a defining characteristic of metals with strong correlations and of insulators.

Calculation of the spin-polarized DOS reveals that Ti_4MnBi_2 may be magnetically ordered. The spin- and orbital-resolved DOS for the two Mn atoms are plotted in Figs. 4(c) and 4(d). A hidden magnetic ordering is revealed, in that only the $d_{x^2-y^2}$ and d_{xy} states are able to sustain spin polarization. Comparing the same d orbitals in Figs. 4(c) and 4(d), it is seen that the sign of the spin magnetic moments

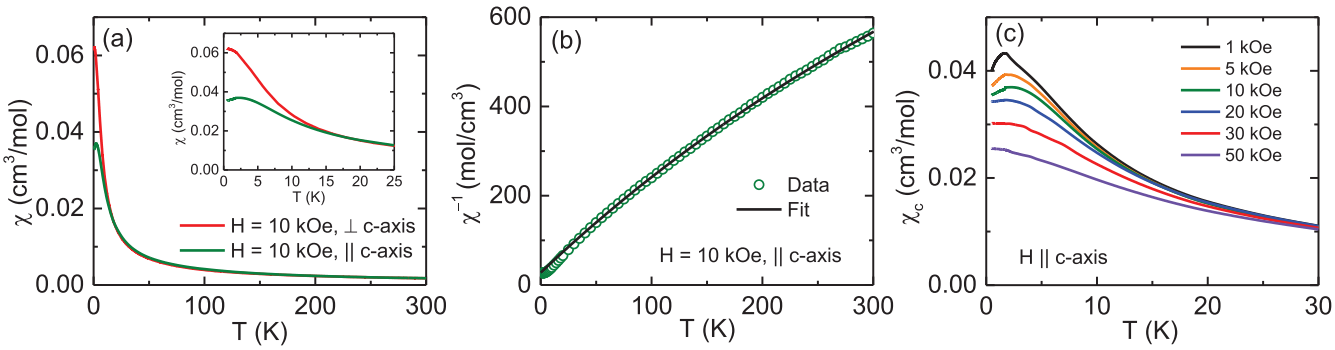

FIG. 5. (a) Temperature dependence of the magnetic susceptibility $\chi = M/H$ of Ti_4MnBi_2. The red data are for a 10 kOe field applied perpendicular to the c-axis, while the green data are for the same field applied along the c-axis. Inset: An expanded view of $\chi(T)$ at low temperatures highlighting its anisotropy. (b) Temperature dependence of χ^{-1} at 10 kOe field applied parallel to the c-axis. Solid curve is the CW fit as described in the text. (c) Temperature dependencies of $\chi_c(T)$ measured at six different fields between 1 and 50 kOe, as indicated. All fields were applied parallel to the c-axis.

of the two intrachain neighboring Mn atoms, represented as Mn-1 and Mn-2, is reversed. Although the total spin magnetic moment on each Mn is small compared to the overall Mn moment, the ESC predicts that AFM ordering will be established on the $d_{x^2-y^2}$ and d_{xy} orbitals.

E. Magnetic properties

The temperature dependence of the magnetic susceptibility $\chi(T)$ of Ti_4MnBi_2 measured with a 10 kOe magnetic field oriented both perpendicular and parallel to the c-axis is plotted in Fig. 5(a). In both field orientations, broad maxima are observed that are centered near 1.9 K. Above $\simeq 15$ K, $\chi_{ab}(T)$ and $\chi_c(T)$ data are nearly identical. The inverse of the susceptibility $\chi^{-1}(T)$ data is well fitted by the CW expression augmented by a temperature-independent contribution χ_0,

$$\chi(T) = \frac{C}{T-\theta_p} + \chi_0, \tag{2}$$

where C is the Curie constant and θ_p is the paramagnetic Weiss temperature. The fitted values of the parameters are as follows: $C = 0.41(2)$ cm^3 K/mol, $\theta_p = -9(3)$ K, and $\chi_0 = 4.8(5) \times 10^{-4}$ cm^3/mol (Table II). The estimated value of the effective paramagnetic moment $\mu_{eff} = \sqrt{8C}$ (assuming $g = 2$) is 1.79(4) μ_B/Mn, which is close to the 1.73 μ_B expected for a spin $S = 1/2$ system. This reduction of the Mn moment from its maximal Hund's rule value can be taken as evidence for an intermediate degree of itineracy of the Mn magnetism in Ti_4MnBi_2. The negative value of θ_p establishes that the dominant interaction in this material is of AFM nature. Within the Heisenberg model of crystallographically equivalent localized spins, the exchange constant(s) can be estimated using $\theta_p = -\frac{S(S+1)}{3k_B}\sum_j J_{ij}$ [43]. Assuming that the dominant exchange J_c couples magnetic moments along the chains where the distance between Mn moments is smallest, we estimate $\theta_p = -J_c/2k_B$ for $S = 1/2$, which leads to $J_c = 18(6)$ K.

The Pauli susceptibility of Ti_4MnBi_2 is estimated using $\chi_{Pauli} = \mu_B^2 \mathcal{D}(E_F) = 7.8(9) \times 10^{-4}$ cm^3/mol for $\mathcal{D}_\gamma(E_F) = 24(3)$ state/eV f.u. is similar to the value of χ_0 (Table II), suggesting the same origin for both. The fact that both $\mathcal{D}_{\chi_0}(E_F) = 14.8$ states/eV f.u. and $\mathcal{D}_\gamma(E_F)$ show a substantial enhancement over $\mathcal{D}_{band}(E_F)$ further suggests the presence of sizable electron correlation effects in Ti_4MnBi_2. The inset of Fig. 5(a) shows that at low temperatures, χ_{ab} measured with the field in the basal plane ($H \perp c$) has a much stronger temperature dependence compared to χ_c when the field is along the c-axis ($H \parallel c$). χ_0 is subtracted from the measured anisotropic susceptibilities to isolate their temperature-dependent parts, which demonstrates that the anisotropy approaches $\sim$2 at 1.9 K. The measurements with $H \parallel c$ are reported for different fields between 1 and 50 kOe in Fig. 5(c). An abrupt slope change in $\chi_c(T)$ measured with $H = 1$ kOe indicates the onset of AFM order at $T_N = 1.9$ K. Increasing magnetic fields broaden and weaken the peak in $\chi_c(T)$, suggesting that the magnetic correlations become progressively short ranged as the field destabilizes AFM order.

The field dependence of the magnetization M provides further information about the magnetic correlations and moment in Ti_4MnBi_2. Isotherms of the magnetization $M(H)$ are shown in Fig. 6(a) for seven different temperatures from 2 to 100 K. The $M(H)$ plots are nonlinear and the nonlinearity becomes more pronounced as the temperature decreases. Isothermal magnetization normalized to the saturation magnetization M/M_{sat} is plotted as a function of the scaled magnetic energy $\mu H/k_B T$ (where $M_{sat} = gS\mu_B = 1$ μ_B considering $S = 1/2$ and $g = 2$) at four different temperatures between 1 and 10 K [Fig. 6(b)]. For comparison, we have also plotted the simulated Brillouin function (BF) for $S = 1/2$, which represents the behavior of localized spins in the paramagnetic regime. It is evident from the plot that the magnitude of M/M_{sat} at any measured value of $\mu H/k_B T$ is significantly reduced compared to the expectations of the BF [Fig. 6(b)]. Apparently, there is a nonsaturating contribution to the magnetization data at low temperatures that results in the positive gradient in the $M(H)$ curves even at the high fields of our measurement. A plausible reason for the observed reduction is the emergence of AFM correlations that also show their signature in the $C_p(T)$ and in the $\chi(T)$ measurements at the low temperatures. To investigate this scenario, we fitted the $M(H)$ data taken in close

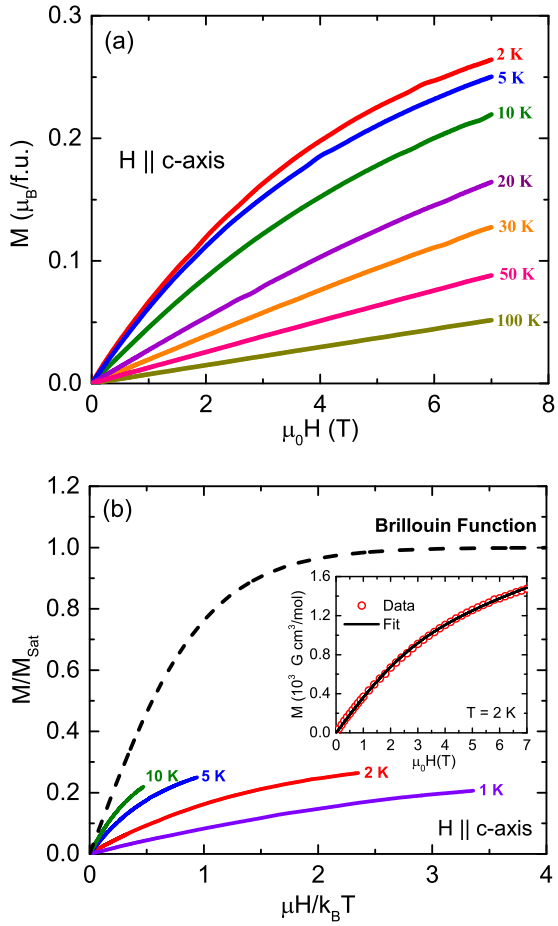

FIG. 6. (a) Isothermal magnetization $M(H)$ measured with the field $H \parallel c$-axis at seven different temperatures, as indicated. (b) Normalized $M/M_{\rm sat}$ plotted as a function of $\mu H/k_{\rm B}T$ at low temperatures, as indicated, where $M_{\rm sat} = gS\mu_{\rm B}$. Simulated Brillouin function with $S = 1/2$ and $g = 2$ is shown by the dashed line. Inset: The fit of the $M(H)$ data at 2 K as described in the text.

proximity ($T = 2$ K) to the magnetic transition temperature ($T_{\rm N} = 1.9$ K) using the expression

$$M(T,H) = fM_{\rm sat}B_S\left[\frac{g\mu_{\rm B}H}{k_{\rm B}T}\right] + \chi_{\rm AFM}H, \qquad (3a)$$

where f is a prefactor to the BF and $\chi_{\rm AFM}$ represents the susceptibility of the antiferromagnetically coupled spins [44]. The BF can be described as [45]

$$B_S(x) = \frac{1}{2S}\left\{(2S+1)\coth\left[(2S+1)\frac{x}{2}\right] - \coth\left(\frac{x}{2}\right)\right\}, \qquad (3b)$$

where $x = g\mu_{\rm B}H/k_{\rm B}T$ and $M_{\rm sat} = N_{\rm A}gS\mu_{\rm B}$. The $M(H)$ data of Ti_4MnBi_2 measured at $T = 2$ K were fitted satisfactorily [inset, Fig. 6(b)] to this expression by varying only two parameters f and $\chi_{\rm AFM}$ and keeping $g = 2$ and $S = 1/2$. As anticipated from Fig. 6(b), the weighting factor f is much smaller than one [$f = 0.146(2)$] and $\chi_{\rm AFM} = 9.8(2) \times 10^{-3}$ cm^3/mol.

This analysis suggests an intermediate degree of localization in Ti_4MnBi_2. The appearance of the term in $M(H)$ that can be described by the BF attests to the presence of reasonably well-defined Mn moments. Unlike an insulator where $f = 1$ and each moment is localized by correlations into a well-defined and long-lived valence state, the observation in Ti_4MnBi_2 that $f \ll 1$ is consistent with the breadth in energy of the Mn states [Fig. 4(b)] where the valence is poorly defined and the Mn d-electrons have a pronounced itinerant character due to hybridization effects. While it is a matter for future work, it is possible that quantum fluctuations associated with either the one-dimensionality of Ti_4MnBi_2 or alternatively to proximity to an electronic localization instability that produces a magnetic moment from a correlated band could contribute additional breadth to the Mn states at the lowest temperatures. One may wonder if the second term $\chi_{\rm AFM}H$ could possibly be associated with the Pauli susceptibility of the conduction carriers. However, $\chi_{\rm AFM}$ is nearly an order of magnitude larger than the value of $\chi_{\rm Pauli}$ (Table II), suggesting that $\chi_{\rm AFM}$ likely reflects the presence of AFM correlations or even long-ranged order that affects the partially localized Mn moments.

Neutron diffraction measurements have been used to search for the presence of magnetic order in Ti_4MnBi_2. Figure 7(a) shows the neutron powder pattern obtained at 0.05 K, where the data were fit using Rietveld refinement. The estimated agreement factor of the fit is $R_{\rm wp} = 4.85\%$, and the diffraction peaks can all be indexed as the nuclear peaks of the crystal structure. Furthermore, as shown in the Fig. S2 of the Supplemental Material [25], there is no indication of additional peaks or temperature dependencies that might suggest the onset of magnetic order between 6.5 and 0.05 K. Neutron diffraction scans were carried out at 2.5 K along selected directions of reciprocal space, using an aligned collection of single crystals. Several weak and broad peaks were observed near the 001 [Fig. 7(b)] and 111 [Fig. 7(c)] positions. Since these data were obtained above the apparent AFM ordering temperature of 1.9 K deduced from the maxima in $C_{\rm p}/T$ and $\chi(T)$, these moments are only correlated over small length scales, poised to turn into true magnetic-diffraction peaks when the temperature drops below $T_{\rm N}$. Since these reflections are forbidden in the $I4/mcm$ space group of Ti_4MnBi_2, it is concluded that the propagation wave vector of the implied magnetic order is either (1,1,1) or (0,0,1). A symmetry analysis was performed using the program SARAh [25,46]. Of the eight irreducible representations appropriate for Ti_4MnBi_2, only one can reproduce the relative intensities of the (001) and (111) diffraction peaks.

The basis vectors imply that the ordered Mn moment lies in the ab-plane, as do the lobes of the associated d_{xy} and $d_{x^2-y^2}$ orbitals. As shown in Fig. 7(d), this magnetic structure has Mn moments that are perpendicular to the c-axis. The Mn moments are antiferromagnetically aligned along the c-axis but ferromagnetically correlated within the ab-plane. Thus, the dominant feature of the magnetic structure of Ti_4MnBi_2 is the presence of AFM order that doubles the chemical unit cell along the c-axis, with the FM order between the chains. The ratio of the structure factors obtained for the (001) and (002) diffraction peaks provides the normalization for the AFM peaks and in this way we obtained an ordered moment of $\simeq 0.05\ \mu_{\rm B}$/Mn. The small ordered moment explains its apparent absence in the powder-diffraction experiment, which would typically only be sensitive to ordered moments $\mu \sim 0.1\ \mu_{\rm B}$. It is significant that the ordered moment $0.05\ \mu_{\rm B}$/Mn

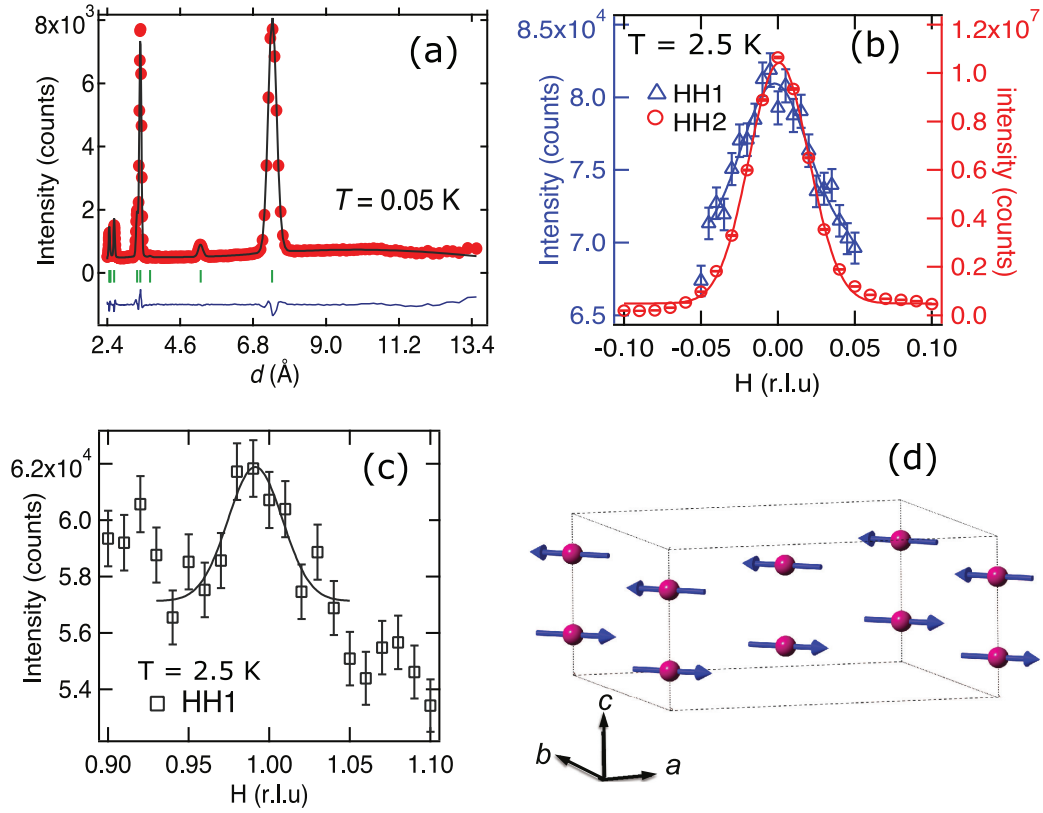

FIG. 7. (a) Rietveld refinement of the neutron powder-diffraction data of Ti_4MnBi_2 measured at 0.05 K. Experimental data points are shown by solid symbols, the black curve through them is a Rietveld analysis fit, green vertical bars indicate nuclear Bragg reflections (space group $I4/mcm$), and the blue curve is the difference between the experimental and the calculated profiles. (b) Single-crystal neutron diffraction data obtained at 2.5 K showing the existence of a weak magnetic peak at (001). The nuclear reflection (002) is also shown for comparison. (c) Another weak magnetic peak (111) is observed in the single-crystal neutron diffraction experiments. Both (001) and (111) reflections are forbidden by the crystal structure of Ti_4MnBi_2. (d) Magnetic structure for Ti_4MnBi_2 determined from representation analysis [25], showing Mn moments with antiferromagnetic alignment along the c-axis and ferromagnetic alignment within the ab-plane. Error bars when indicated are statistical in origin and represent one standard deviation.

is only 3% of the 1.79 μ_B/Mn CW moment, suggesting that the magnetic fluctuations are very strong in Ti_4MnBi_2, to the point that they are almost overwhelming magnetic order.

IV. DISCUSSION

The specific heat [Fig. 3(b)] and the magnetic susceptibility [Fig. 5(a)] measurements have broad peaks centered near 1.9 K that provide corroborating evidence for the magnetic order that has been found in the neutron diffraction measurements. The entropy contained in the specific heat peak [Fig. 3(c)] is about 9% of $R\ln 2$/Mn, providing a measure of the staggered moment that is possibly more accurate than that found in the single-crystal neutron diffraction measurements, which were obtained for $T \simeq T_N$ where the staggered moment would not yet be fully developed as at $T \ll T_N$. The qualitative conclusion is unaffected, that the ordered moment is much smaller than the CW moment of 1.79 μ_B/Mn. The breadth of the peaks in the single-crystal neutron diffraction measurements as well as in the temperature dependencies of the specific heat and magnetic susceptibility are suggestive that true long-ranged order does not occur in Ti_4MnBi_2, rather the correlations remain finite ranged due to strong fluctuations. These fluctuations could potentially be the result of magnetic frustration that originates with the low dimensionality implied by the chainlike crystal structure of Ti_4MnBi_2. However, the ESC raise the alternative possibility that Ti_4MnBi_2 could be naturally tuned to an instability of the Fermi surface itself, leading to the emergence of a tiny Mn moment from a correlated band of Mn states.

Resistivity and heat capacity measurements establish that Ti_4MnBi_2 is inherently metallic and this conclusion is confirmed by the ESC. The calculations find that the DOS at the E_F is dominated by Ti states, which are substantially hybridized. The comparison to experiment indicates that these Ti-based states have moderate electronic correlations. The DOS at the E_F determined from the Sommerfeld coefficient $D_\gamma(E_F) = 24$ states/(eV f.u.) is enhanced by a factor of 3.2 relative to that determined from the ESC $D_{band}(E_F) =$ 7.4 states/(eV f.u.), suggesting substantial electronic correlations that are not captured by the ESC. The Kadowaki-Woods ratio $R_{KW} = 0.34\ \mu\Omega\,\text{cm mol}^2\text{J}^{-2}\text{K}^2$ is much smaller than the value of $10\ \mu\Omega\,\text{cm mol}^2\text{J}^{-2}\text{K}^2$ that is typical of the highly correlated heavy electron compounds, but is similar to the value of $0.3\ \mu\Omega\text{cm mol}^2\text{J}^{-2}\text{K}^2$ that is reported for Pd and other transition-metal-based compounds [36]. The Sommerfeld-

Wilson ratio R_W is given by $R_W = \pi^2/3(k_B^2/\mu_B^2)(\chi_0/\gamma)$, where k_B is Boltzmann's constant and μ_B is the Bohr magneton. In an uncorrelated Fermi liquid $R_W = 1$, but R_W is greater than 1 if FM correlations are present. Using the values $\gamma = 57\,\mathrm{mJ/mol\,K^2}$ and $\chi_0 = 4.8 \times 10^{-4}\ \mathrm{cm^3/mol}$, we find that $R_W = 0.6(2)$, ruling out appreciable FM correlations in Ti_4MnBi_2.

There are two intertwined scenarios that have emerged in our study of the metallic Ti_4MnBi_2. The first is whether the Mn moments are spatially localized or itinerant. If the latter, then we could interpret the weak magnetic order to be the consequence of a magnetic moment that has emerged from a band with a critical degree of correlations. The second consideration is whether the one-dimensionality implied by the crystal structure with its chains of Mn atoms confers a 1D character to the magnetic and electronic structures. These two themes will next be discussed at some length. Our conclusion, however, will be that more investigations are needed to scrutinize the relevance of these two themes to the underlying physics of Ti_4MnBi_2.

Our analysis of the electronic correlations described above allows for the possibility that Mn moments are not only itinerant in Ti_4MnBi_2, but they may also be critical in that the bandlike states from which they emerge have just enough correlations to produce a long-lived Mn moment, albeit a small one. A range of magnetic characters is possible for Mn in metals that reflects the interplay of local Hund's and Coulomb interactions, which tend to localize magnetic moments on the Mn sites, with the hybridization of the Mn states, reflected in an effective bandwidth. When the on-site interactions are very strong and the hybridization weak, robust insulators like LaMnPO [42], $CaMn_2Sb_2$ [47], and $BaMn_2As_2$ [40,48,49] occur where nearly full Hund's rule moments are found. When the hybridization is strong as in metallic MnX (X = P, As, Sb, Bi) [50–52], MnSi [53], YMn_2 [54], and $HfMnGa_2$ [55], residual on-site interactions can induce a Mn moment within the correlated electron bands that can be substantially weaker than the Hund's rule values. Assuming that the bandwidth reflects only Mn-Mn hybridization, a Mn moment emerges from the band for a critical value of hybridization that occurs for Mn-Mn spacings near 2.5 Å, antiferromagnetism and growing Mn moments are found for intermediate values of Mn-Mn spacing between $2.5 - 2.8$ Å, while fully localized moments and strong FM character are found for well-separated Mn ions with Mn-Mn spacings larger than 2.9 Å [56]. The nearest Mn-Mn spacing in Ti_4MnBi_2 is 2.5 Å along the chain direction and, in this scheme, Ti_4MnBi_2 might be expected to be on the verge of an electronic transition that would produce a somewhat localized moment, possibly leading to weak AFM order. These expectations are upheld by the ESC, where the similarity of the Mn state energy and bandwidth attests to a modest level of correlations, with just sufficient localization to provide a CW moment of 1.79 μ_B/Mn. The observations of weak AFM order and staggered moments that are much smaller than the Hund's rule moments are suggestive that Ti_4MnBi_2 naturally forms close to the instability that leads to the formation of an AFM quantum critical point, where moments form and simultaneously order at $T = 0$. The ESC support this finding, where the Mn DOS is found to be spin polarized, supporting a small staggered moment, in qualitative agreement with the value inferred from the entropy S_{mag} associated with AFM order and from the staggered moment found in neutro diffraction measurements. It is interesting to note that the staggered moment found by ESC is associated only with the $d_{x^2-y^2}$ and d_{xy} orbitals, while the remaining spectral weight associated with the Mn d-electrons forms a broad band centered near -2.5 eV, with a band width of approximately 3 eV. The lobes of these orbitals lie in the plane perpendicular to the Mn-chain axis, in agreement with the magnetic structure deduced from the neutron diffraction measurements. The central question is where to place Ti_4MnBi_2 on the spectrum of itineracy that is possible for magnetic moments in metals. Electron spectroscopy techniques will address this question by testing the results of the DFT calculations and will assess whether the Mn moments are itinerant and contained in the Fermi surface or localized and thus excluded from the Fermi surface.

The crystal structure of Ti_4MnBi_2 features well-separated chains of Mn atoms, suggesting that 1D physics may be relevant to our understanding of this remarkable material. However, it is not yet known whether the electronic and magnetic structures bear the fingerprints of one-dimensionality, such as pronounced anisotropy of the electronic structure or the observation of fractionalized excitations. The experimental work carried out so far in Ti_4MnBi_2 is consistent with the presence of strong fluctuations that limit the magnitude of the ordered moment and suppress AFM order to a lower temperature relative to the Weiss temperature. At this stage, it is difficult to establish whether those fluctuations originate from a 1D character of Ti_4MnBi_2, or from emerging moments in a correlated band, or from a mixture of these two effects. Nonetheless, it is interesting to consider the ways in which electronic correlations, familiar to us in 3D systems, may affect the lowest energy excitations in 1D systems. By analogy, it seems likely that the ESC in 1D systems provide essential information regarding the states that are involved in bonding, the stability of magnetic moments, and whether there is an insulating gap or not. Similarly, there is a separation in scales between these high-energy states where dimensionality plays little role and the fundamental excitations that are found at the lowest energies, where the 1D character is of paramount importance. In most spin chain systems studied so far [3,5–10], their insulating character implies that onsite Hund's and Coulomb interactions are very strong compared to hybridization. It follows that charge excitations are profoundly gapped at high energies and temperature, although any spinons or holons present at low energies can be gapped or not, depending on the anisotropy of the underlying XXZ Hamiltonian or the strength of the interchain coupling [1]. In this case, we expect two different Fermi surfaces for the spinons and holons.

Alternatively, if the bandwidth of states with mobile charge is comparable to the strength of the Coulomb interactions in organic 1D conductors, as is potentially the case for Ti_4MnBi_2, they are rendered metallic in the sense that the 3D ESC carried out in these compounds predict that there is no insulating gap. Organic 1D conductors such as TTF-TCNQ are examples of Tomonaga-Luttinger liquids, where the fundamental excitations are not electron-like quasiparticles but

gapless and fractionalized excitations of spin and charge. ARPES measurements carried out on TTF-TCNQ accordingly find that the lowest energy excitations are spinons and holons [16] and not the electronic quasiparticles of the Fermi liquid state expected in 3D metals. Multiple bands may be important in Ti_4MnBi_2 and this raises the possibility that there may be multiple Fermi surfaces for the spinons and holons, as well as quasiparticles, depending on the strength of interband coupling.

The role of interactions in 1D systems remains a matter of debate. Residual interactions in the Tomonaga-Luttinger state of the 1D organic conductors are sufficient to drive spin-density-wave order, Peierls instabilities and even unconventional superconductivity [14,15]. Long-ranged order necessarily results from interchain coupling, but we are interested mainly in the possibility that these interactions could be sufficiently strong and sufficiently short ranged that Mott-like physics can be realized in 1D systems, where the application of nonthermal variables like pressure, doping, or magnetic field can drive zero-temperature electronic instabilities that are analogous to the Mott-Hubbard transition found in 2D [13] and 3D [57] systems. In 3D systems, the stabilization of moments in metals is described within two different paradigms and we ask whether aspects of these scenarios are appropriate for understanding interacting 1D systems in general, and Ti_4MnBi_2 in particular. In the delocalized case, magnetic moments are induced by interactions in a band of delocalized states, and the moment bearing electrons continue to be included in the Fermi surface. The results reported here suggest that the magnetic character of Ti_4MnBi_2 can be understood in this way, although we concede that accurately reproducing local interactions is notoriously difficult in ESC. If this conclusion is correct, then Ti_4MnBi_2 is a more strongly interacting analog of TTF-TCNQ and its 1D relatives. In the localized case, the Coulomb interactions are strong enough to localize moment-bearing electrons, which are not contained in the Fermi surface. The coexistence of a 1D chain of moments with spinon and holon excitations, coexisting with a separate Fermi surface associated with the conduction electrons would be a more exotic outcome for Ti_4MnBi_2, likely to already have been realized in the metallic spin chain compound Yb_2Pt_2Pb [11]. It is fair to say that it is uncertain at this point whether the Mn d-electron states responsible for the magnetism in Ti_4MnBi_2 are localized or delocalized, how many Fermi surfaces are present, and of what type (spinon, holon, or quasiparticle). Although the crystal structure of Ti_4MnBi_2 with its Mn chains is evocative, it is only the observation of fractionalized excitations from ARPES, resonant inelastic x-ray scattering or inelastic neutron scattering measurements that will determine whether Ti_4MnBi_2 is truly a 1D system. In any case, it is certain that Ti_4MnBi_2 is a unique system that demands further exploration, possibly as a bridge between localized moment spin chains and 1D metals with correlations.

V. CONCLUSION

We have investigated the structural, magnetic, electrical transport, and thermal properties of a previously unexplored compound Ti_4MnBi_2 that contains 1D chains of Mn spins running along the crystallographic c-axis. Our experimental results, along with the results of ESC, establish that this material has a ground state with moderately strong electronic correlations, leading to Fermi liquid behavior at low temperatures. AFM order with small staggered moments is observed at 1.9 K, signaling that spatial and temporal fluctuations nearly overwhelm the tendency to order. These fluctuations may reflect proximity of Ti_4MnBi_2 to an electronic instability where correlations lead for moment formation itself or they may be the consequence of weak interchain interactions among 1D chains of Mn moments that just barely outweigh the fluctuations. Future investigations will address the pertinence of these scenarios and may likely provide determination whether the 1D character implied by the crystal structure controls the electronic and magnetic behaviors or chains of Mn moments do not carry much relevance to the physics of this exciting material. Even at this relatively early stage of understanding, Ti_4MnBi_2 is of importance as one of only a few 1D systems that are metallic while being the first member of a potentially larger and previously unexplored family of 1D systems.

ACKNOWLEDGMENTS

We thank O. Prakash, W. J. Gannon, G. A. Sawatzky, I. Affleck, and D. C. Johnston for helpful discussions. The work at Texas A&M University was supported by the National Science Foundation through Grant No. NSF-DMR-1807451. H.W. and X.Q. acknowledge support from NSF under Award No. DMR-1753054. Portions of this research were conducted with the advanced computing resources provided by Texas A&M High Performance Research Computing. The identification of any commercial product or trade name does not imply endorsement or recommendation by the National Institute of Standards and Technology.

[1] T. Giamarchi, *Quantum Physics in One Dimension*, (Oxford University Press Inc., New York, 2004).

[2] B. Lake, A. M. Tsvelik, S. Notbohm, D. A. Tennant, T. G. Perring, M. Reehuis, C. Sekar, G. Krabbes, and B. Büchner, Confinement of fractional quantum number particles in a condensed-matter system, Nat. Phys. **6**, 50 (2009).

[3] M. Mourigal, M. Enderle, A. Klopperpieper, J. S. Caux, A. Stunault, and H. M. Ronnow, Fractional spinon excitation sin the quantum Heisenberg antiferromagnetic chain, Nat. Phys. **9**, 435 (2013).

[4] J. Schlappa, U. Kumar, K. J. Zhou, S. Singh, M. Mourigal, V. N. Strocov, A. Revcolevschi, L. Patthey, H. M. Ronnow, S. Johnston, and T. Schmitt, Probing multi-spin excitations outside of the two-spinon continuum in the antiferromagnetic spin chain cuprate Sr_2CuO_3, Nat. Commun. **9**, 5394 (2018).

[5] S. Kadota, I. Yamada, S. Yoneyama, and K. Hirakawa, Formation of one-dimensional antiferromagnet in $KCuF_3$ with the perovskite structure, J. Phys. Soc. Jpn. **23**, 751 (1967).

[6] B. Lake, D. A. Tennant, C. D. Frost, and S. E. Nagler, Quantum criticality and universal scaling of a quantum antiferromagnet, Nat. Mater. **4**, 329 (2005).

[7] J. C. T. Lee, S. Yuan, S. Lal, Y. I. Joe, Y. Gan, S. Smadici, K. Finkelstein, Y. Feng, A. Rusydi, P. M. Goldbart, S. L. Cooper, and P. Abbamonte, Two-stage orbital order and dynamical spin frustration in $KCuF_3$, Nat. Phys. **8**, 63 (2012).

[8] E. Pavarini, E. Koch, and A. I. Lichtenstein, Mechanism for Orbital Ordering in $KCuF_3$, Phys. Rev. Lett. **101**, 266405 (2008).

[9] C. Kim, A. Y. Matsuura, Z.-X. Shen, N. Motoyama, H. Eisaki, S. Uchida, T. Tohyama, and S. Maekawa, Observation of Spin-Charge Separation In One-Dimensional $SrCuO_2$, Phys. Rev. Lett. **77**, 4054 (1996).

[10] J. Schlappa, K. Wohlfeld, K. J. Zhou, M. Mourigal, M. W. Haverkort, V. N. Strocov, L. Hozoi, C. Monney, S. Nishimoto, S. Singh, A. Revcolevschi, J.-S. Caux, L. Patthey, H. M. Rønnow, J. van den Brink, and T. Schmitt, Spin–orbital separation in the quasi-one-dimensional Mott insulator Sr_2CuO_3, Nature **485**, 82 (2012).

[11] L. S. Wu, W. J. Gannon, I. A. Zaliznyak, A. M. Tsvelik, M. Brockmann, J.-S. Caux, M. S. Kim, Y. Qiu, J. R. D. Copley, G. Ehlers, A. Podlesnyak, and M. C. Aronson, Orbital-exchange and fractional quantum number excitations in an f-electron metal, Yb_2Pt_2Pb, Science **352**, 1206 (2016).

[12] Y. Jompol, C. J. B. Ford, J. P. Griffiths, I. Farrer, G. A. C. Jones, D. Anderson, D. A. Ritchie, T. W. Silk, and A. J. Schofield, Probing spin-charge separation in a Tomonaga-Luttinger liquid, Science **325**, 597 (2009).

[13] K. Kanoda and R. Kato, Mott physics in organic conductors with triangular lattices, Annu. Rev. Condens. Matter Phys. **2**, 167 (2011).

[14] D. Jerome, Organic superconductors: When correlations and magnetism walk in, J. Supercond. Nov. Magn. **25**, 633 (2012).

[15] A. Ardavan, S. Brown, A. Kagoshima, K. Kanoda, K. Kuroki, H. Mori, M. Ogata, S. Uji, and J. Wosnitza, Recent topics of organic superconductors, J. Phys. Soc. Jpn. **81**, 011004 (2012).

[16] R. Claessen, M. Sing, U. Schwingenschlogl, P. Blaha, M. Dressel, and C. S. Jacobsen, Spectroscopic Signatures of Spin-Charge Separation in the Quasi-One-Dimensional Organic Conductor TTF-TCNQ, Phys. Rev. Lett. **88**, 096402 (2002).

[17] A. E. Sikkema, I. Affleck, and S. R. White, Spin Gap in a Doped Chain, Phys. Rev. Lett. **79**, 929 (1997).

[18] H. Tsunetsugu and M. Sigrist, The ground-state phase diagram of the one-dimensional Kondo lattice model, Rev. Mod. Phys. **69**, 809 (1997).

[19] A. M. Tsvelik and O. M. Yevtushenko, Quantum Phase Transition and Protected Ideal Transport in a Kondo Chain, Phys. Rev. Lett. **115**, 216402 (2015).

[20] D. J. Schimmel, A. M. Tsvelik, and O. M. Yevtushenko, Low energy properties of the Kondo chain in the RKKY regime, New. J. Phys. **18**, 053004 (2016).

[21] I. Khait, P. Azaria, C. Hubig, U. Schollwock, and A. Auerbach, Doped Kondo chain, a heavy Luttinger liquid, Proc. Nat. Acad. Sci. **115**, 5140 (2018).

[22] C. G. Richter, W. Jeitschko, B. Künnen, and M. H. Gerdes, The ternary titanium transition metal bismuthides Ti_4TBi_2 with $T =$ Cr, Mn, Fe, Co, and Ni, J. Solid State Chem. **133**, 400 (1997).

[23] R. Rytz and R. Hoffmann, Chemical bonding in the ternary transition metal bismuthides Ti_4TBi_2 with $T =$ Cr, Mn, Fe, Co, and Ni, Inorg. Chem. **38**, 1609 (1999).

[24] J. Rodríguez-Carvajal, Recent advances in magnetic structure determination by neutron powder diffraction, Physica B **192**, 55 (1993); see also www.ill.eu/sites/fullprof/.

[25] See Supplemental Material at http://link.aps.org/supplemental/10.1103/PhysRevB.102.014406 for a discussion of the powder x-ray and neutron-diffraction data as well as the symmetry analysis for determination of magnetic structure.

[26] J. W. Lynn, Y. Chen, S. Chang, Y. Zhao, S. Chi, W. Ratcliff, B. G. Ueland, and R. W. Erwin, Double focusing thermal triple axis spectrometer at the NCNR, J. Research NIST **117**, 61 (2012).

[27] R. Oishi, M. Yonemura, Y. Nishimaki, S. Torii, A. Hoshikawa, T. Ishigaki, T. Morishima, K. Mori, T. Kamiyama, Rietveld analysis software for J-PARC, Nucl. Instr. Meth. Phys. Res. A **600**, 94 (2009).

[28] R. Oishi-Tomiyasu, M. Yonemura, T. Morishima, A. Hoshikawa, S. Torii, T. Ishigaki, T. Kamiyama, Application of matrix decomposition algorithms for singular matrices to the Pawley method in Z-Rietveld, J. Appl. Cryst. **45**, 299 (2012).

[29] P. Hohenberg and W. Kohn, Inhomogeneous electron gas, Phys. Rev. **136**, B864 (1964).

[30] W. Kohn and L. J. Sham, Self-consistent equations including exchange and correlation effects, Phys. Rev. **140**, A1133 (1965).

[31] G. Kresse and J. Furthmüller, Efficient iterative schemes for ab initio total-energy calculations using a plane-wave basis set, Phys. Rev. B **54**, 11169 (1996).

[32] P. E. Blochl, Projector augmented-wave method, Phys. Rev. B **50**, 17953 (1994).

[33] J. P. Perdew, K. Burke, and M. Ernzerhof, Generalized Gradient Approximation Made Simple, Phys. Rev. Lett. **77**, 3865 (1996).

[34] J. Klimeš, D. R. Bowler, and A. Michaelides, Chemical accuracy for the van der Waals density functional, J. Phys.: Condens. Matter **22**, 022201 (2010).

[35] S. L. Dudarev, G. A. Botton, S. Y. Savrasov, C. J. Humphreys, and A. P. Sutton, Electron-energy-loss spectra and the structural stability of nickel oxide: An LSDA+U study, Phys. Rev. B **57**, 1505 (1998).

[36] A. C. Jacko, J. O. Fjærestad, and B. J. Powell, A unified explanation of the Kadowaki–Woods ratio in strongly correlated metals, Nat. Phys. **5**, 422 (2009).

[37] N. Marzari, A. A. Mostofi, J. R. Yates, I. Souza, and D. Vanderbilt, Maximally localized Wannier functions: Theory and applications, Rev. Mod. Phys. **84**, 1419 (2012).

[38] X. Qian, J. Li, L. Qi, C. Z. Wang, T. L. Chan, Y. X. Yao, K. M. Ho, and S. Yip, Quasiatomic orbitals for ab initio tight-binding analysis, Phys. Rev. B **78**, 245112 (2008).

[39] Y. P. Yin, K. Haule, and G. Kotliar, Kinetic frustration and the nature of the magnetic and paramagnetic states in iron pnictides and iron chalcogenides, Nat. Mater. **10**, 932 (2011).

[40] D. E. McNally, S. Zellman, Z. P. Yin, K. W. Post, Hua He, K. Hao, G. Kotliar, D. Basov, C. C. Homes, and M. C. Aronson, From Hunds insulator to Fermi liquid: Optical spectroscopy study of K doping in $BaMn_2As_2$, Phys. Rev. B **92**, 115142 (2015).

[41] N. S. Sangeetha, A. Pandey, Z. A. Benson, and D. C. Johnston, Antiferromagnetism in trigonal $SrMn_2AS_2$ and $CaMn_2As_2$ single crystals, Phys. Rev. B **94**, 094417 (2016).

[42] D. E. McNally, J. W. Simonson, K. W. Post, Z. P. Yin, M. Pezzoli, G. J. Smith, V. Leyva, C. Marques, L. DeBeer-Schmitt, A. I. Kolesnikov, Y. Zhao, J. W. Lynn, D. N. Basov, G. Kotliar, and M. C. Aronson, Origin of the charge gap in LaMnPO, Phys. Rev. B **90**, 180403(R) (2014).

[43] D. C. Johnston, Magnetic Susceptibility of Collinear and Noncollinear Heisenberg Antiferromagnets, Phys. Rev. Lett. **109**, 077201 (2012).

[44] A Weiss temperature θ_c was used as a fit parameter in the fitting of $M(H)$ data by the BF. However, since the best fit results in $\theta_c = 0$ within the error bars, θ_c was not included in the expression used for the final fitting.

[45] R. J. Goetsch, V. K. Anand, A. Pandey, and D. C. Johnston, Structural, thermal, magnetic, and electronic transport properties of the $LaNi_2(Ge_{1-x}P_x)2$ system, Phys. Rev. B **85**, 054517 (2012).

[46] A. S. Wills, A new protocol for the determinations of magnetic structures using simulated annealing and representational analysis (SARAh), Physica B **287**, 680 (2000).

[47] J. W. Simonson, G. J. Smith, K. Post, M. Pezzoli, J. J. Kistner-Morris, D. E. McNally, J. E. Hassinger, C. S. Nelson, G. Kotliar, D. N. Basov, and M. C. Aronson, Magnetic and structural phase diagram of $CaMn_2Sb_2$, Phys. Rev. B **86**, 184430 (2012).

[48] J. An, A. S. Sefat, D. J. Singh, and M.-H. Du, Electronic structure and magnetism in $BaMn_2As_2$ and $BaMn_2Sb_2$, Phys. Rev. B **79**, 075120 (2009).

[49] Y. Singh and D. C. Johnston, Magnetic, transport, and thermal properties of single crystals of the layered arsenide $BaMn_2As_2$, Phys. Rev. B **79**, 094519 (2009).

[50] H. Okuda, S. Senba, H. Sato, K. Shimada, H. Namatame, and M. Taniguchi, Electronic structure of MnSb and MnP, J. Electron Spectrosc. **101–103**, 657 (1999).

[51] K. V. Shanavas, D. Parker, and D. J. Singh, Theoretical study on the role of dynamics on the unusual magnetic properties in MnBi, Sci. Rep. **4**, 7222 (2014).

[52] J. Okabayashi, M. Mizuguchi, K. Ono, M. Oshima, A. Fujimori, H. Kuramochi, and H. Akinaga, Density-dependent electronic structure of zinc-blende-type MnAs dots on GaAs(001) studied by in situ photoemission spectroscopy, Phys. Rev. B **70**, 233305 (2004).

[53] F. Carbone, M. Zangrando, A. Brinkman, A. Nicolaou, F. Bondino, E. Magnano, A. A. Nugroho, F. Parmigiani, Th. Jarlborg, and D. van der Marel, Electronic structure of MnSi: The role of electron-electron interactions, Phys. Rev. B **73**, 085114 (2006).

[54] H. Yamaoka, N. Tsujii, I. Jarrige, Y. Takahashi, J. Chaboy, H. Oohashi, K. Handa, J. Ide, T. Tochio, Y. Ito, T. Uruga, and H. Yoshikawa, Electronic structure of YMn_2 and $Y_{0.96}Lu_{0.04}Mn_2$ studied by x-ray emission spectroscopy, Phys. Rev. B **80**, 115110 (2009).

[55] C. Marques, Y. Janssen, M. S. Kim, L. Wu, S. X. Chi, J. W. Lynn, and M. C. Aronson, $HfFeGa_2$ and $HfMnGa_2$: Transition-metal-based itinerant ferromagnets with low Curie temperatures, Phys. Rev. B **83**, 184435 (2011).

[56] J. M. D. Coey, *Magnetism and Magnetic Materials* (Cambridge University Press, Cambridge, 2010).

[57] G. Kotliar and D. Vollhardt, Strongly correlated materials: Insights from dynamical mean field theory, Phys. Today **57**(3), 53 (2004).